Fluid Dynamics & Materials Processing
DOI:10.32604/fdmp.2020.09509
Article

A Numerical Investigation on the Characteristics of the Radial Force in a Cycloid Gerotor Pump

Lingzhi Yu[1], Yunqing Gu[1,*], Jiegang Mou[1], Denghao Wu[1], Zhenfu Chen[2] and Yun Ren[3]

[1]College of Metrology & Measurement Engineering, China Jiliang University, Hangzhou, 310018, China
[2]College of Mechanical Engineering, Zhejiang University of Technology, Hangzhou, 310014, China
[3]Zhijiang College, Zhejiang University of Technology, Shaoxing, 312030, China
[*]Corresponding Author: Yunqing Gu. Email: guyunqing@cjlu.edu.cn
Received: 24 December 2019; Accepted: 04 August 2020

Abstract: In order to improve the performances of a cycloid gerotor pump, the variations of the radial force induced by different rotating speeds and outlet pressures are analyzed numerically. Using the numerical simulations as a basis, an improved oil inlet and outlet groove structure is proposed. The results show that the radial force decreases with the decrease of the outlet pressure and of the rotor speed. Compared with the original model, the large-end oil inlet line and pressure line of the new oil groove are claw-shaped. This configuration can effectively weaken the pressure changes inside the gerotor pump and reduce accordingly the radial force on the inner rotor.

Keywords: Cycloid gerotor pump; radial force; oil groove structure; pressure distribution

1 Introduction

Gerotor pump has many advantages like compact structure, small size and light-weight [1–3]. It is an important part of an automobile engine [4] and construction machinery lubrication system [5]. Its main function is to pump oil and provide a steady stream of motor oil for the lubrication system. Gerotor pumps can be divided into internal gear pump and external gear pump according to their structure. Cycloid gerotor pumps are widely used in automotive lubrication systems [6] because of their compact structure, high volumetric efficiency and low cost. The main disadvantage of the gerotor pump is the large internal leakage and radial force. The radial force on the internal rotor is composed of the radial force generated by the liquid pressure along the circumference of the inner rotor and the radial force generated by the meshing of the rotor. The periodic pressure shock in the rotor pump cavity can aggravate the radial force of the gerotor pump. The excessive radial force will cause the insufficient of rotor axis's rigidity, worse the meshing of the rotor, and affect the accuracy of the meshing. Eventually, it will reduce the life of the rotor pump [7,8].

At present, the research on cycloid gerotor pumps mainly focuses on analyzing the rotor's profile of cycloid gerotor pumps [9] and improving the volumetric efficiency [10,11]. The research on the radial force of gerotor pumps is mainly focused on the derivation of theoretical formulas. For example, Xing [12] deduced the calculation formula of the radial force of the cycloid pump by analyzing the radial force

composition of the cycloid pump and taking the involute gear pump as a reference. Li et al. [13,14] deduced the calculation formulas of the maximum radial force on the gear shaft of the internal-meshing gear pump and the maximum bending moment of the gear teeth through computer drawing. Although there has been some research on the radial force of gerotor pumps, there is less research on improving the pulsation of radial force under different working conditions.

This article takes the cycloid gerotor pump as the research object, and uses the methods of numerical simulation to study the influence of rotating speed and outlet pressure on the radial force of the gerotor pump [15,16], analyzes the internal flow state of the gerotor pump, and delves into the causes and position of extreme values of radial force pulsations. Based on the above analysis, a new oil groove structure is proposed to reduce the radial force on the internal rotor in the gerotor pump.

2 Numerical Calculation Method of Cycloid Gerotor Pump Flow Field

2.1 Computing Models and Meshing

D30 cycloid gerotor pump was selected as research object, and its design parameters are that: outer diameter of external rotor D_2 = 69.7 mm, inner diameter of external rotor d_2 = 42.7 mm, outer diameter of internal rotor D_1 = 52.6 mm, Inner diameter of internal rotor d_1 = 32.85 mm, thickness h = 22 mm, teeth number of internal rotor Z_1 = 4, teeth number of external rotor Z_2 = 5, rated speed n = 1500 r/min, outlet pressure P_2 = 0.5 MPa. The three-dimensional fluid domain model of the cycloidal rotor pump is established by using CATIA software, as shown in Fig. 1. Pumplinx is used for meshing and non-constant constant simulation.

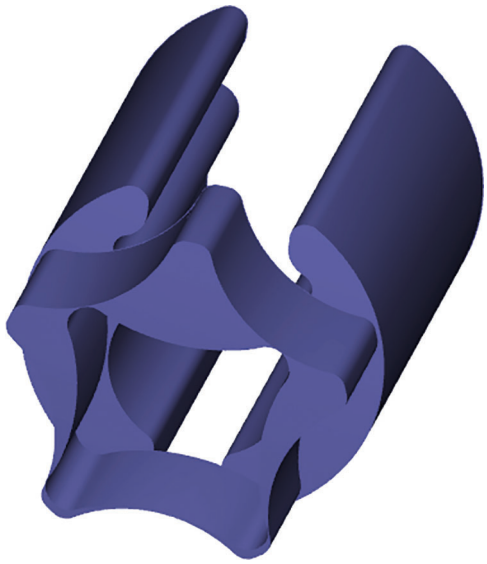

Figure 1: Schematic diagram of calculation model of cycloid gerotor pump

Because there is a very small gap, 0.1 mm, between the internal and external rotors, the grid of this gap should be refined to accord with the calculation accuracy. However, such a small grid will lead to a sharp increase of the number of grid points, and the solving time will be too long. In the view of the above problems, structured meshing of the rotor and oil groove is taken into consideration to save the number of meshes. PumpLinx includes an automated Cartesian grid generator. It can quickly generate high-quality meshes that match the CFD solver and can be solved efficiently. The grid generator uses a geometry Conformal Adaptative Binary-tree (CAB) algorithm. Near the geometric boundary, the mesh

generator automatically splits the large mesh, integrates the small mesh to fit the geometric surface shape and the geometric boundary line, so as to capture the details of the geometric boundary. This method can efficiently use the smallest grid to resolve detail features.

In order to take into account the reliability of numerical simulation and the time it takes to calculate, it is necessary to select an appropriate number of grid points. When the correlation between the outlet flow of the cycloidal rotor pump and the number of grid points is not large, it can be regarded as grid-independent. Five sets of grids with different scales were used to perform numerical simulation under the working condition of $n = 3000$ r/min and $P_2 = 0.5$ MPa. The simulated outlet flows corresponding to the number of different grids are shown in Tab. 1. It can be seen from the table that when the grid number is greater than 221250, the volumetric efficiency of the cycloidal rotor pump is basically stable, and the error is within 1%. Finally, the total number of meshes is 242369. The meshes of the internal and external rotors are divided into 12 layers. The meshing is shown in Fig. 2. Volumetric efficiency in a pump refers to the percentage of actual fluid flow out of the pump compared to the flow out of the pump without leakage.

Table 1: Mesh sensitivity analysis

Mesh number	Volumetric efficiency (%)
221250	87.44
242369	87.60
271023	87.82

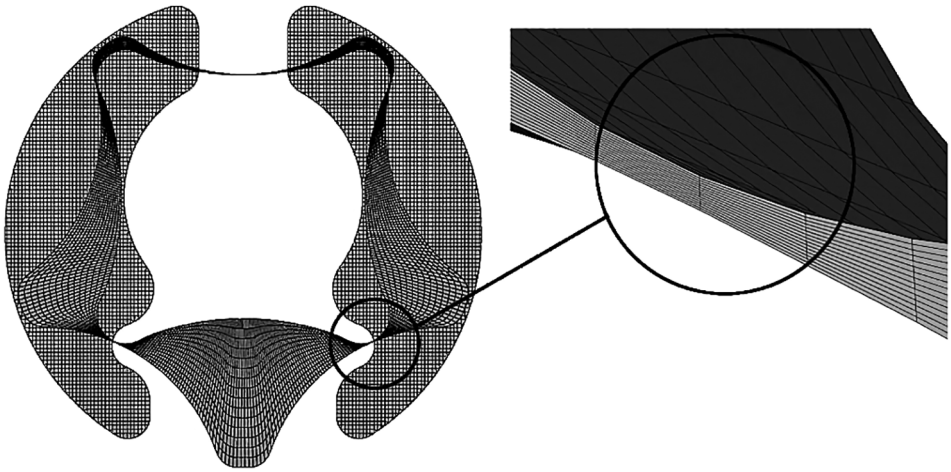

Figure 2: Meshing of cycloid gerotor pump

2.2 Mathematical Model

1. Governing equations

The oil of the cycloid gerotor pump is an isothermal fluid, so it does not need to be described by the energy conservation equation. The law of conservation of mass of the cycloid gerotor pump is expressed as: The mass of fluid flowing into the control body per unit time is equal to the sum of the mass of fluid flowing out of the control body and the increase in the mass of fluid in the control body. The mass balance equation [17] is:

$$\frac{\partial(u_x)}{\partial x}+\frac{\partial(u_y)}{\partial y}+\frac{\partial(u_z)}{\partial z}=0 \tag{1}$$

where u_x is fluid velocity in the x direction, u_y is fluid velocity in the y direction, u_z is fluid velocity in the z direction.

The fluid inside the cycloid gerotor pump is an incompressible viscous fluid and the momentum conservation equation [17] is:

$$\rho\frac{\partial(u_i)}{\partial t}+\rho\frac{\partial(u_iu_j)}{\partial x_j}=\frac{\partial}{\partial x_j}\left[\mu\left(\frac{\partial u_i}{\partial x_j}+\frac{\partial u_j}{\partial x_i}\right)\right]-\frac{\partial p}{\partial x_i}+f_i \tag{2}$$

where u_i is fluid three-dimensional velocity component, x_i is each coordinate component, f_i is external source, μ is hydrodynamic viscosity, ρ is fluid density, t is time.

2. Turbulence model

In this paper, the RNG k-ε turbulence model is selected to simulate the three-dimensional unsteady flow of a cycloidal rotor pump. The RNG k-ε turbulence model not only fully considers the rotation and swirling conditions in the fluid flow of the cycloidal rotor pump, but also can accurately simulate the flow near the wall of the cycloidal rotor pump.

The turbulent kinetic energy equation used in the RNG k-ε turbulence model [18] is:

$$\frac{\rho\partial(k)}{\partial t}+\rho\frac{\partial(ku_j)}{\partial x_j}=\frac{\partial}{\partial x_j}\left(\alpha_k\mu_e\frac{\partial k}{\partial x_j}\right)+\rho(P_k-\varepsilon) \tag{3}$$

$$\rho\frac{\partial(\varepsilon)}{\partial t}+\rho\frac{\partial(\varepsilon u_j)}{\partial x_j}=\frac{\partial}{\partial x_j}\left(\alpha_\varepsilon\mu_e\frac{\partial \varepsilon}{\partial x_j}\right)+\rho\frac{\varepsilon}{k}\left(C_{1\varepsilon}^{*}P_k-C_{2\varepsilon}\varepsilon\right) \tag{4}$$

In this equation, $C_{1\varepsilon}^{*}=C_{1\varepsilon}-\frac{\eta(1-\eta/\eta_0)}{1+\beta\eta^3}$, $\eta=\left(2E_{ij}\cdot E_{ij}\right)^{1/2}\frac{k}{\varepsilon}$, $E_{ij}=\frac{1}{2}\left(\frac{\partial u_i}{\partial x_j}+\frac{\partial u_j}{\partial x_i}\right)$. μ_e is the effective viscosity coefficient. E_{ij} is the time-average strain rate. Model constant: $\alpha_k=\alpha_\varepsilon=1.39$, $C_{1\varepsilon}=1.42$, $C_{2\varepsilon}=1.68$, $\eta_0=4.377$, $\beta=0.012$.

2.3 Numerical Method

Pressure-based solution is used to solve basic equations. The pressure-velocity coupling equation is solved by PRESTO algorithm [19]. The pressure term is discretized in SIMPLE format [20], and the remaining terms are discretized in first-order upwind style.

2.4 Setting of Condition

In order to examine the influence of the speed and outlet pressure on the radial force of the rotor pump, five speeds of n = 1000, 1500, 2000, 2500, 3000 r/min and five different outlet pressures P_2 = 0.1, 0.2, 0.3, 0.4, 0.5 MPa were selected for numerical calculation.

Boundary conditions include: The end faces of the inlet and outlet tanks of the pump are the boundary conditions of pressure inlet and pressure outlet, the inlet pressure is 1 standard atmospheric pressure, and the other surfaces are set to the boundary conditions of the wall surface. The convergence accuracy during the calculation is 1×10^{-3}. The temperature change of the oil is not considered in the calculation, and the energy equation is not added to the model. The oil density is 800 kg/m^3 and the saturation pressure is 400 Pa.

2.5 Validation of Numerical Method

Select 8 operating conditions, n = 2000, 3000 r/min, P_2 = 0.2, 0.3, 0.4, 0.5 MPa, to perform numerical simulation on the cycloidal rotor pump and obtain the external characteristic parameters of the cycloidal rotor pump, that is, the outlet flow Q_2. In Fig. 3, it is can be found that the numerical simulation performance curve is consistent with the measured performance curve by comparing experimental and simulated values. The outlet flow increases with the increase of the speed, and is basically proportional to the speed. This is because the increase in speed directly causes more oil in the interdental volume to be pumped out of the oil channel per unit time. Outlet flow decreases with increasing outlet pressure. This is because the increase in outlet pressure leads to an increase in the pressure difference with the inlet pressure, that is, the pressure difference at the rotor gap also increases accordingly, resulting in an increase in leakage at the gap, which reduces the outlet flow. In addition, the numerical simulation of the outlet flow rate is higher than the test value under various operating conditions, because the simulation does not consider the actual rotor end face leakage and axial leakage caused by the deviation. Comparing the test value with the simulation value, it can be seen that the agreement is generally good, and the deviation of calculation is about 3%, which indicates that the accuracy of the numerical simulation is acceptable.

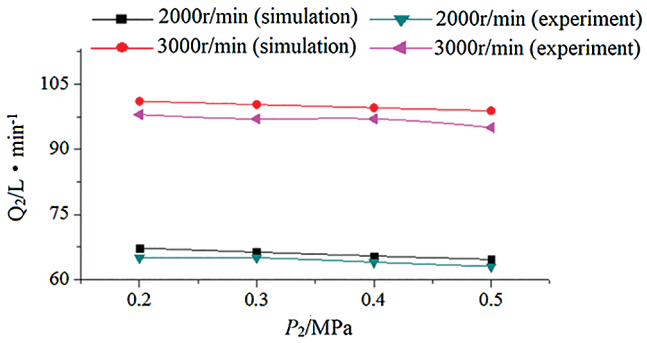

Figure 3: External characteristic curve of Gerotor pump

3 Analysis of Characteristics of Radial Force

3.1 The Effect of Outlet Pressure on Radial Force

The higher the speed of the gerotor pump, the more the radial force on the internal rotor. In order to intuitively show the change of radial force of the internal rotor under different outlet pressures, take n = 3000 r/min to analyze the change of radial force under 5 types of outlet pressure. As shown in Fig. 4, Fig. 4a is a change curve of a radial force F_x received in a lateral direction and Fig. 4b is a change curve of a radial force F_y received in a longitudinal direction. It can be seen from Fig. 4 that F_x and F_y both decrease as the outlet pressure decreases, but their sensitivity to the outlet pressure is different. F_x varies sharply with the size of the outlet pressure and changes linearly. Each time the outlet pressure decreases by 0.1 MPa, F_x decreases by 20%, and the pulsation amplitude of F_x also decreases accordingly. However, the change in outlet pressure has little effect on F_y. For each decrease of 0.1 MPa in outlet pressure, F_y decreases by about 6%. It can be seen that the change in outlet pressure has a greater impact on F_x. The reason is that the size of F_x is determined by the pressure difference between the oil inlet and the oil outlet. So, the effect on F_x is greater. F_y is mainly determined by the pressure difference in the y-direction, that is, the trapped oil pressure of the meshing volume of the rotor, so its correlation with the outlet pressure is small.

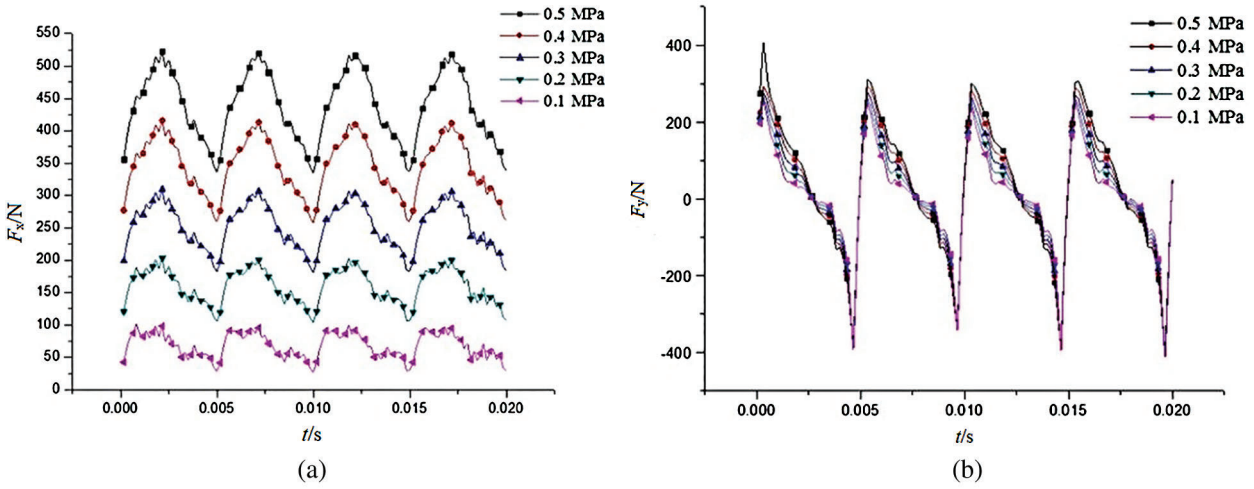

Figure 4: The radial force of internal rotor under different outlet pressure. (a) F_x and (b) F_y

3.2 Effect of Speed on Radial Force

It can be known from Fig. 4 that at a certain speed, the greater the P_2, the greater the radial force of the internal rotor. Therefore, in the process of analyzing the influence of the speed, analyze the change of radial force under five kinds of speed under the condition of P_2 = 0.5 MPa. It is shown in Fig. 5 that F_x, F_y both become smaller with reduction of n, and the amplitude of pulsation also becomes smaller. When n is small, the change of n has a small effect on F_x and F_y, but as n increases, the change becomes drastic. When n decreases sequentially from 3000, 2500, 2000, 1500, 1000 r/min, reduction rate of F_x were 5.51%, 4.74%, 3.89%, 2.97%; and reduction rate of F_y were 20.35%, 18.91%, 17.98%, 16.11%. It can be seen that the change of n has a greater impact on F_y.

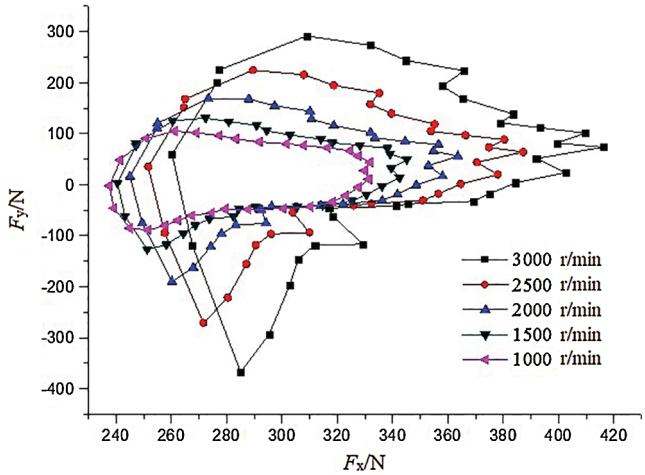

Figure 5: Radial force of internal rotor at different speed

3.3 Analysis of Extreme Position of F_x and F_y

Fig. 6 shows the radial force pulsation of the internal rotor at the condition of n = 3000 r/min and P_2 = 0.5 MPa. It can be seen from Fig. 6 that the amplitude of the pulsation of F_x is much smaller than that of F_y and F_x is a positive value. In addition to the large amplitude, the value of F_y has sudden changes from negative to

positive. Radial force shocks and sudden changes can seriously affect the stiffness of the pump shaft. When F_x reaches the maximum value, F_y is about zero. At this time, the rotor is symmetrically distributed along the y-axis, so F_y is close to zero. when F_x reaches the minimum value, F_y changes from negative to positive and it is in this time that the maximum volume between the teeth is changed from oil absorption to oil extraction. The pressure distribution cloud diagrams of the rotor position where F_x and F_y take extreme values in Fig. 6 are shown in Figs. 7 and 8.

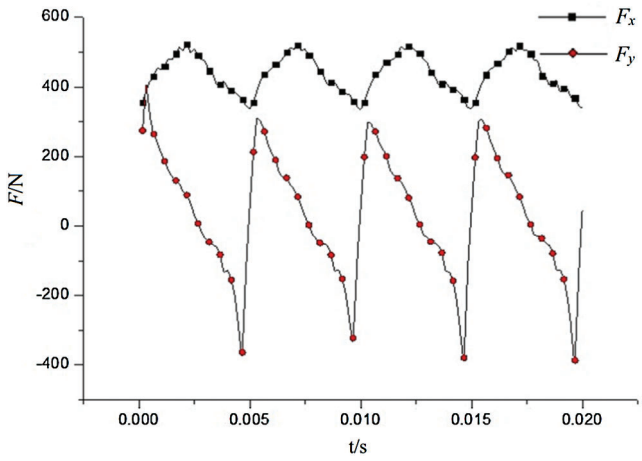

Figure 6: Radial force of internal rotor when n = 3000 r/min, P_2 = 0.5 MPa

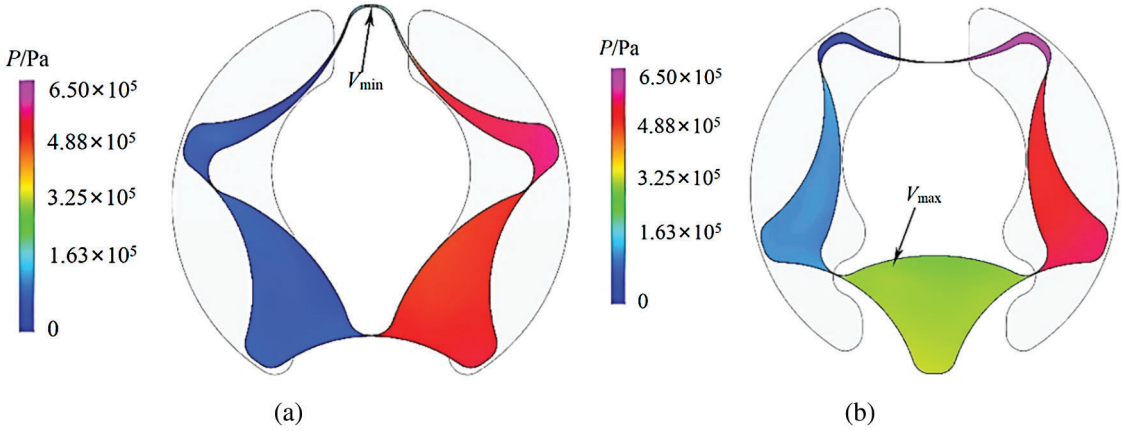

Figure 7: Pressure distribution of F_x extreme position. (a) When F_x is minimum and (b) When F_x is maximum

In Fig. 7, the position of the extreme value of F_x is shown. Fig. 7a shows the pressure distribution when F_x is the smallest, and Fig. 7b shows the pressure distribution when F_x is the largest. As can be seen from Fig. 7, the position where F_x reaches the minimum value is the position where the rotor turns to the maximum inter-tooth area V_{max}. At this time, the oil absorption process has been completed, but oil pressure has not been performed. The negative pressure in the oil absorption area has been eliminated. The pressure in the oil drainage area has not increased. The pressure difference between the oil discharge area and the oil absorption area is not too big. So F_x reaches the minimum value. The position where F_x reaches the maximum value is the position where the rotor turns to the minimum inter-tooth area V_{min}. At

this time, the oil pressure process is completed. The pressure of the oil discharge zone reaches the Maximum, the pressure in the oil absorption zone is relatively low, the pressure difference between the oil discharge zone and the oil absorption zone are symmetrical along with the y-axis distribution, so $F_y = 0$. It can be clearly seen that the high-pressure area near the oil discharge cavity in Fig. 7b is significantly more than the high-pressure area in Fig. 7a, and the pressure is greater; the low-pressure area near the oil inlet cavity in Fig. 7b is also significantly more than the low-pressure area in Fig. 7a, and the negative pressure is greater.

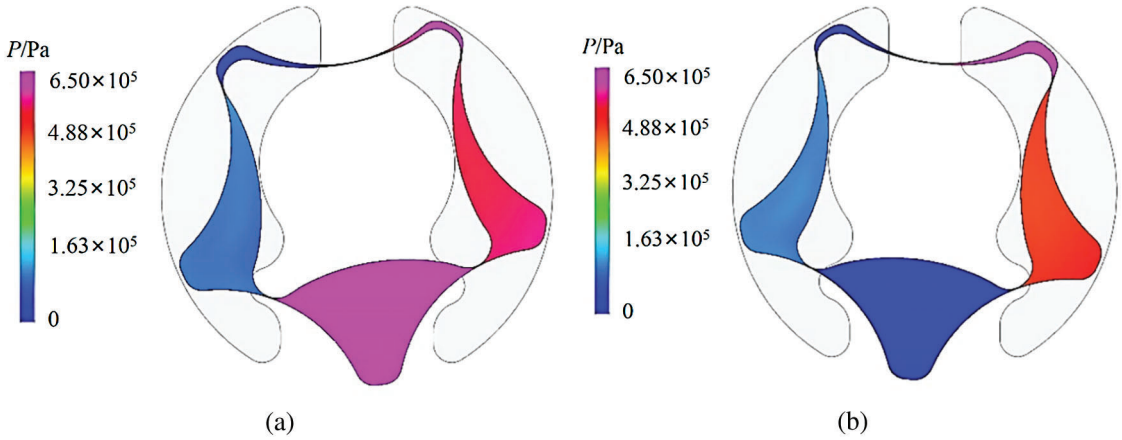

Figure 8: Pressure distribution of F_y extreme position. (a) Negative maximum of F_y and (b) Positive maximum of F_y

In Fig. 8, the position where F_y extremes occur is showed. The Fig. 8a is the pressure distribution when F_y is at the maximum in the negative direction, and Fig. 8b is the pressure distribution when F_y is at the maximum in the positive direction. As can be seen from Fig. 8, the position where F_y reaches the negative maximum value is the position where the rotor is about to turn to the maximum inter-tooth area V_{max}. At this time, the inter-tooth area continues to increase, resulting in a decrease in pressure, and the oil in the oil groove is too late to fill the inter-tooth area. When the inter-tooth area is close to V_{max}, the pressure drops to the lowest value, so that the negative pressure difference along the y-axis reaches the maximum, so F_y reaches the negative maximum value; the position where F_y reaches the positive maximum value is that the rotor has just passed the maximum inter-tooth area V_{max}. The area between the teeth is constantly decreasing, resulting in an increase in pressure, and this part of the high-pressure oil is too late to be discharged through the oil groove, and the oil pressure rises to the highest value so that the pressure difference in the positive direction along the y-axis reaches the maximum. Therefore, F_y reaches a positive maximum. From the pressure distribution in the figure, it can be seen that during the process of the rotor changing from the position shown in Fig. 8a to the position shown in Fig. 8b, the maximum inter-tooth volume suddenly changed from extremely low negative pressure to extremely high positive. This is because when the maximum inter-tooth volume connects with the drain groove, the high-pressure fluid in the groove flows back into the inter-tooth volume, causing a sudden rise in pressure. At the same time, this part of the return fluid does not form an effective flow rate, which causes fluctuations in the outlet flow rate.

4 The Improvement of Inlet and Outlet Oil Groove

Based on the above analysis of the locations and causes of the extreme values of F_x and F_y, an improved structure of the inlet and outlet groove is proposed. As shown Fig. 9, the improved large-end oil inlet line and oil pressure line are claw-shaped, so that when the cycloid gerotor pump sucks oil, the oil in the oil inlet

groove can fill the inter-tooth volume earlier and when the pump pressurizes oil, the high-pressure oil can discharge the inter-tooth volume earlier. To conclude, the new structure can alleviate the sudden pressure charge in the flow field of the gerotor pump and reduce the radial force.

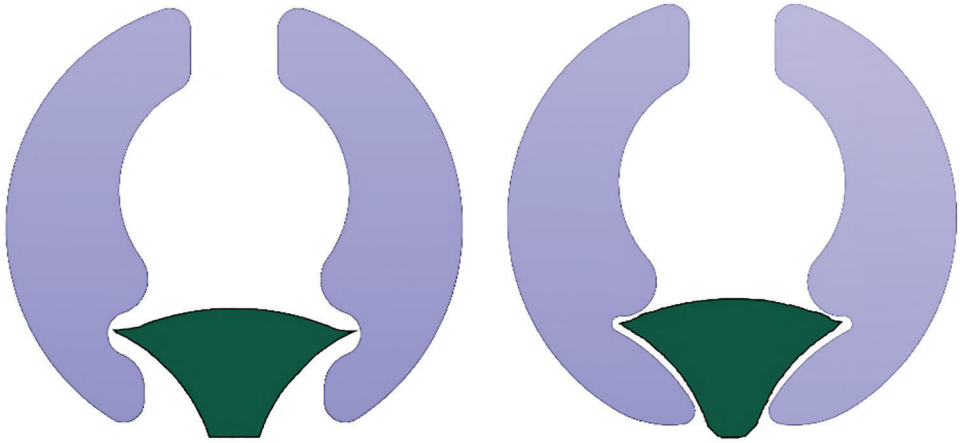

Figure 9: Improved oil groove structure. (a) Before improvement and (b) After improvement

Fig. 10 is a comparison diagram of the radial force before and after the oil groove is improved. It can be seen from Fig. 10 that F_x does not change much before and after the model is improved. From the above analysis, it is known that F_x is mainly affected by the outlet pressure. The outlet pressure determines the pressure difference between the oil inlet area and the oil outlet area. The extreme value of F_y in the improved model has decreased significantly, and the fluctuation is more stable. The drop position is mainly the peak point of F_y, a process of the sudden change from negative to positive so that the impact on the rotor shaft is reduced. According to the data analysis, the positive maximum value of F_y decreases by 35.8%, the negative maximum value of F_y decreases by 69.1%, and the overall pulsation amplitude decreases by 53.8%, indicating that the improved oil groove structure has a significant relief effect on F_y.

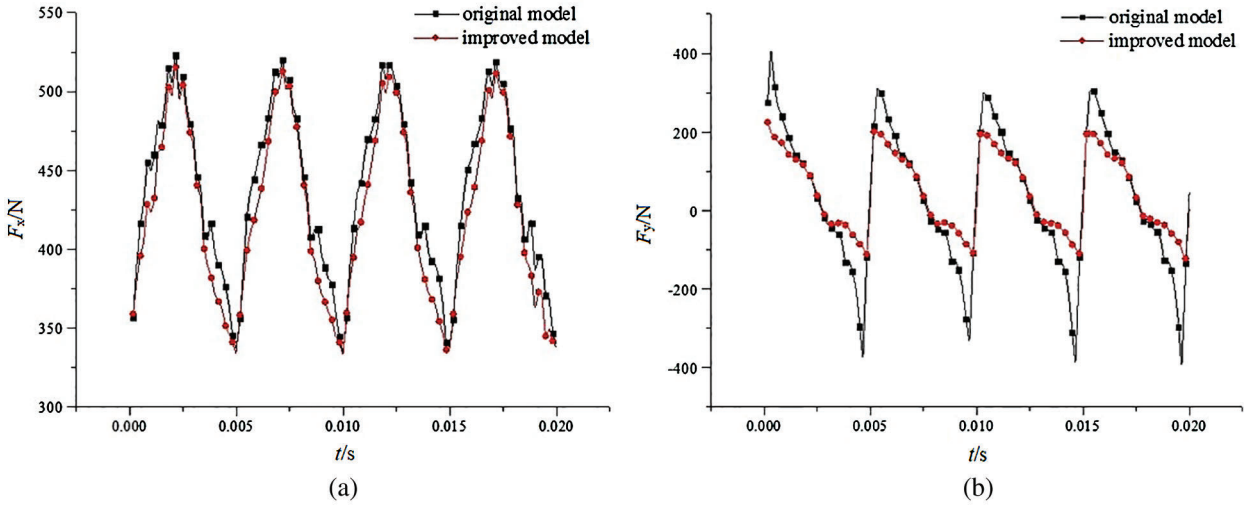

Figure 10: The comparison of radial force before and after advance. (a) F_x and (b) F_y

Because the improvement effect of F_x is not large, the flow field analysis is not performed at its corresponding time, and the analysis is mainly performed on the flow field at the extreme time of F_y. Fig. 11 shows the pressure distribution of the improved model. As can be seen from Fig. 11, when F_y reaches the negative maximum value, that is, the rotor is about to turn to the maximum inter-tooth area V_{max}, the inter-tooth volume is constantly increasing, and the pressure is continuously decreasing. The improved claw-shaped oil groove can ensure the entire process of oil can be in contact with the volume between the teeth so that the oil can fully fill the interdental volume and avoid the formation of excessive negative pressure. Compared with Fig. 8a, it can be clearly seen that the flow field pressure in the V_{max} region has increased, and decreased the negative maximum value of F_y. When F_y reaches the positive maximum value, that is, the rotor has just passed the maximum inter-tooth area V_{max}, the inter-tooth volume is continuously reduced, and the pressure is continuously increased. The improved claw-shaped oil groove can be connected to the inter-tooth volume earlier so that the compressed high-pressure oil can be discharged from the oil groove in time to avoid the formation of excessively high pressure. Compared with Fig. 8b, it can be clearly seen that the flow field pressure in the V_{max} region has reduced, thereby reducing the positive maximum value of F_y.

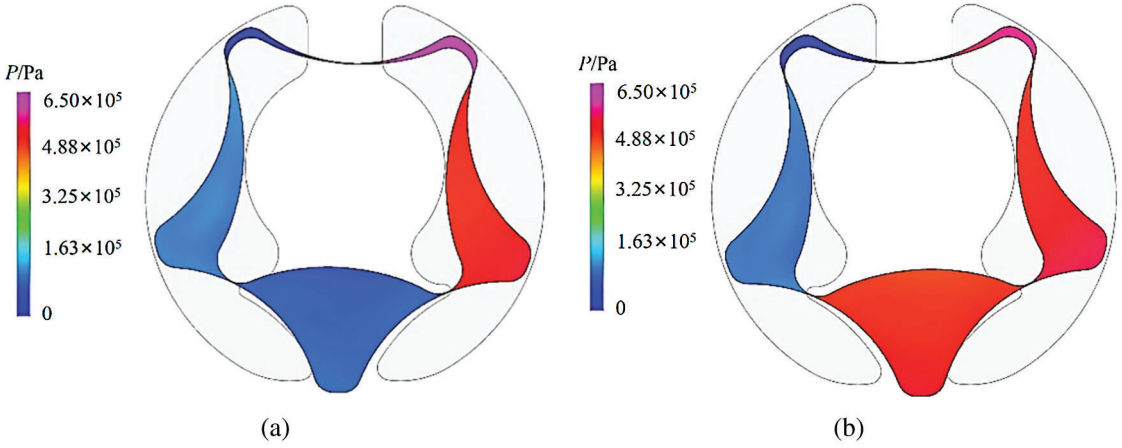

Figure 11: Pressure distribution of the improved model. (a) The negative maximum of F_y and (b) The positive maximum of F_y

5 Conclusion

The radial forces of F_x and F_y on the rotor shaft both decrease as the outlet pressure decreases, and F_x changes sharply with the magnitude of the outlet pressure, which changes linearly, and the change in outlet pressure has little effect on F_y. F_x and F_y both increase with the increase of n, and change dramatically as the increase of n. The effect of n on F_x is small, but the effect on F_y is large.

The position where F_x reaches the minimum value is the position where the rotor is turned to the maximum inter-tooth area V_{max}, and the position where F_x reaches the maximum value is the position where the rotor is turned to the minimum inter-tooth area V_{min}. The position where F_y reaches the negative maximum value is the position where the rotor is about to turn to the maximum inter-tooth area V_{max}, and the position where F_y reaches the positive maximum value is the position where the rotor has just passed the maximum inter-tooth area V_{max}.

Based on the analysis of the radial force of the cycloid gerotor pump, we come up with an improved oil inlet and outlet groove with a claw-shaped large-end oil inlet line and oil pressure line. After the model improving, F_x changes a little. The extreme value of F_y after the improvement is significantly reduced,

and the fluctuation is more stable. The positive maximum value of F_y decreases by 35.8%, the negative maximum value of F_y decreases by 69.1%, and the overall pulsation amplitude decreases by 53.8%. It shows that the improved oil groove structure has an obvious effect on decreasing F_y.

Funding Statement: This work was supported by the Zhejiang Provincial Natural Science Foundation of China (No. LY19E050003); and the National Natural Science Foundation of China (No. 51779226).

Conflicts of Interest: The authors declare that they have no conflicts of interest to report regarding the present study.

References

1. Mao, H. Y., Li, G. X., Yang, B., Zhang, J. Y. (2003). Design in cycloid rotor pump. *Powder Metallurgy Technology, 21(5),* 282–286.
2. Jacazio, G., Martin, D. A. (2016). Influence of rotor profile geometry on the performance of an original low-pressure gerotor pump. *Mechanism and Machine Theory, 100,* 296–312. DOI 10.1016/j.mechmachtheory.2016.02.012.
3. Antoniak, P., Stryczek, J. (2018). Visualization study of the flow processes and phenomena in the external gear pump. *Archives of Civil and Mechanical Engineering, 18(4),* 1103–1115. DOI 10.1016/j.acme.2018.03.001.
4. Liu, H., Lee, J. (2016). Development of combined trochoidal profile of a gerotor pump. *Journal of Applied Mathematics and Physics, 4(1),* 28–32. DOI 10.4236/jamp.2016.41005.
5. Suresh, K. M., Manonmani, K. (2010). Computational fluid dynamics integrated development of gerotor pump inlet components for engine lubrication. *Proceedings of the Institution of Mechanical Engineers, Part D: Journal of Automobile Engineering, 224(12),* 1555–1567. DOI 10.1243/09544070JAUTO1594.
6. Mattia, B., Emiliano, M. (2020). On the assessment of lumped parameter models for gear pump performance prediction. *Simulation Modelling Practice and Theory, 99,* 102008. DOI 10.1016/j.simpat.2019.102008.
7. Shen, H. D., Li, Z. Q., Qi, L. L., Qiao, L. (2018). A method for gear fatigue life prediction considering the internal flow field of the gear pump. *Mechanical Systems and Signal Processing, 99,* 921–929. DOI 10.1016/j.ymssp.2016.09.022.
8. Stryczek, J., Bednarczyk, S., Biernacki, K. (2014). Strength analysis of the polyoxymethylene cycloidal gears of the gerotor pump. *Archives of Civil and Mechanical Engineering, 14(4),* 647–660. DOI 10.1016/j.acme.2013.12.005.
9. Wang, Y. Z., Ren, S. Y., Li, Y. (2019). Design and manufacturing of a novel high contact ratio internal gear with a circular arc contact path. *International Journal of Mechanical Sciences, 153,* 143–153.
10. Tian, P., Huang, J., Shi, W., Zhou, L. (2019). Optimization of a centrifugal pump used as a turbine impeller by means of an orthogonal test approach. *Fluid Dynamics & Materials Processing, 15(2),* 139–151. DOI 10.32604/fdmp.2019.05216.
11. Gu, Y. Q., Yu, S. W., Mou, J. G., Wu, D. H., Zheng, S. H. (2020). Research progress on the collaborative drag reduction effect of polymers and surfactants. *Materials, 13(2),* 444. DOI 10.3390/ma13020444.
12. Xing, L. H., Duan, J. Z. (2014). Theoretical analysis and calculation of cycloidal gear pump radial force. *Journal of Mechanical Transmission, 38(9),* 106–108.
13. Li, H. W., Gao, S. Z. (2007). Mechanics analysis of gear axis for internal gear pumps. *Chinese Hydraulics & Pneumatics, 5,* 73–75.
14. Li, H. W., Cui, L. L., Cheng, X. C. (2009). Flexibility analysis of gear shaft of internal gear pumps. *Machine Tool & Hydraulics, 37(9),* 116–118.
15. Liu, K., Xu, L., Yang, B., Liu, Y. (2019). Numerical simulation of external helical gear high-pressure pump with CFD. *Journal of Drainage and Irrigation Machinery Engineering, 37(4),* 307–312.
16. Cheng, Z. Y., Wang, Y. L., Wang, Y. G., Nie, Q. (2019). On the application of a mobile grid technology to computational fluid dynamics. *Fluid Dynamics & Materials Processing, 15(4),* 357–366. DOI 10.32604/fdmp.2019.07843.
17. Wang, F. J. (2020). *Analysis method of flow in pumps & pumping stations*. Beijing: China Water & Power Press.

18. Lu, J., Cheng, J. (2018). Numerical simulation analysis of energy conversion in hydraulic turbine of hose irrigator JP75. *Journal of Drainage and Irrigation Machinery Engineering, 36(5),* 448–453.
19. Shmueli, H., Ziskind, G., Letan, R. (2010). Melting in a vertical cylindrical tube: Numerical investigation and comparison with experiments. *International Journal of Heat and Mass Transfer, 53(19–20),* 4082–4091. DOI 10.1016/j.ijheatmasstransfer.2010.05.028.
20. Sujeet, K. S., Prashant, S., Pradyumna, G. (2011). Evaluation of numerical schemes using different simulation methods for the continuous phase modeling of cyclone separators. *Advanced Powder Technology, 22(2),* 209–219. DOI 10.1016/j.apt.2010.11.009.